

On Advection, Diffusion, Bubbles, and Beer

Math 714 Final Project

Carsen Grote, Mark Han

December, 2023

1 Introduction

Under adequate conditions a fluid containing dissolved gas can become supersaturated and begin to discharge gas into the surrounding air. In nature and industrial processes, supersaturation of a fluid occurs when the surrounding air undergoes a rapid pressure or temperature change. The governing law is that of Henry's Law which states that the amount of dissolved gas within a liquid is proportional to its partial pressure in the air above the liquid [1]. A common example of this phenomenon is opening a can of a carbonated beverage. In the sealed can the fluid and adjacent gas is under sufficient concentration such that the gas remains dissolved [2]. Opening the can rapidly depressurizes the air neighboring the fluid, breaking Henry's Law, and gas instantly begins to leave the fluid. Gas escapes by diffusing across the air-liquid interface and through the formation of gas bubbles on surfaces in the fluid that grow and rise to the surface [3]. In this project we build a computational model that simulates the decay of gas in a two dimensional supersaturated fluid through diffusion across the air-surface interface. We consider the transportation of gas via advection and diffusion in a fluid with a constant velocity field as described below. The role of container geometry, initial gas concentration, and the number of circulation cells in encouraging or limiting gas loss are investigated. Before developing the model we first describe the nature of the constant velocity field in the fluid and give grounds for using such a velocity field.

Upon reaching supersaturation, gas bubbles begin to nucleate and grow at many sites within the fluid. This can occur in multiple ways: bubble nucleation in the bulk fluid; bubble nucleation on an immersed surface; and bubble nucleation prompted by existing air pockets inside a cellulose fiber on the container surface [4]. The first mechanism, known as homogeneous bubble nucleation, is not seen in common supersaturated fluids like carbonated beverages as it is energetically expensive, requiring the fluid to be significantly

supersaturated [5]. For nucleation on a surface, known as heterogeneous nucleation, the critical energy required for bubble nucleation scales inversely with the contact angle made by the bubble and the surface, requiring much less energy to nucleate a bubble than homogeneous nucleation [5]. Even less energetically costly is the last mechanism as an air bubble already exists in the fiber and gas simply needs to diffuse into it until it becomes enlarged and escapes the fiber to rise to the surface [4]. A combination of the latter two mechanisms are responsible for the nucleation and growth of bubbles in common supersaturated fluids.

The supersaturation ratio, $S(t) = (\bar{c}(t)/c_s - 1)$, measures the volume averaged gas concentration, $\bar{c}(t)$, compared to a critical value c_s given by Henry's Law [6]. As the fluid loses gas, $S(t)$ decays down to a minimum value S_{mc} at which bubbles no longer form on the immersed container walls. While $S(t) > S_{mc}$, the constant growth and rise of bubbles in the fluid drive a large scale circulation flow similar to that of intrinsic convection in particle sedimentation [4]. This flow continually replenishes the surface boundary layer with concentration from the liquid bulk as shown in figure (1), dramatically enhancing gas loss across the air-surface interface. Therefore, while $S(t) > S_{mc}$, it is reasonable to consider a large scale circulation flow given by a constant, axisymmetric velocity field to model the gas loss of a supersaturated fluid. Depending on the properties of the container such as the side lengths and locations of the bubble nucleation sites, more than one circulation cell may emerge.

While our computational model uses the circulation flow created by the bubbles, it does not account for the gas loss due to the bubbles reaching the surface. Although the bubbles growing and reaching the surface may appear to the eye as the main driver of the gas loss, experiments have shown that only $\sim 20\%$ of carbon dioxide molecules escape in the form of bubbles in glasses of Champagne [7]. Therefore our model's simulation of the direct diffusion of molecules across the air-surface interface will give insight into the process responsible for the far majority of the gas loss in a supersaturated fluid.

2 Mathematical Model

Consider a two dimensional container with length L , height H , and the interior of the container given by (x, z) for $-L/2 < x < L/2$ and $-H < z < 0$. We are interested in the dynamics of the gas concentration c with respect to the location in the container $\mathbf{x} = (x, z)$ and time t , $c(\mathbf{x}, t)$. The dissolved gas concentration is assumed to behave

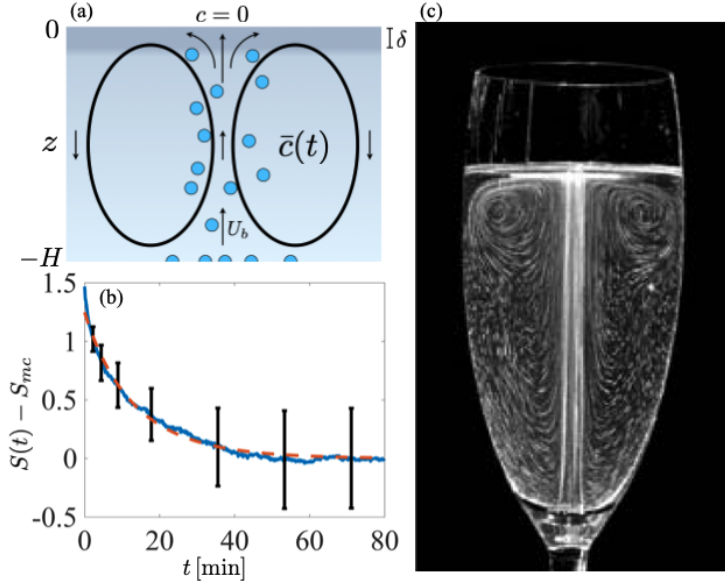


Figure 1: (a) Schematic of the large-scale circulation flow driven by bubbles forming on and detaching from the bottom of the container. Taken from [6]. (b) The CO₂ gas supersaturation ratio, minus a stationary minimum value below which bubbles do not form, $S(t) - S_{mc}$, for carbonated water in a rectangular container. Taken from [6]. (c) A glass of champagne with CO₂ bubbles driving a large scale, single cell circulation flow. Taken from [4].

according to an advection-diffusion equation for an incompressible fluid,

$$c_t = -\mathbf{u} \cdot \nabla c + D \nabla^2 c, \quad (1)$$

where \mathbf{u} is the fluid velocity, D is the diffusion coefficient for the gas in the fluid, and c_t is the time derivative of the concentration. The natural boundary conditions are $\mathbf{n} \cdot \nabla c = 0$ on the bottom and side walls of the container, with \mathbf{n} the outward-pointing normal vector. Assuming a negligibly small concentration of the corresponding gas in the adjacent air above the fluid (like that of CO₂ in air), and assuming that Henry's Law is constantly satisfied at the air-surface interface, we require that $c(z = 0, t) = 0$ at the top surface.

As discussed above, the velocity field is driven by the bubbles with the number of circulation cells determined by the container geometry and location of the nucleation sites. A flow field consisting of N circulation cells spanning the horizontal measure of the container, L , and depth, H , has the form $\mathbf{u} = u_x \hat{\mathbf{x}} + u_z \hat{\mathbf{z}}$, where

$$u_x = \frac{-U_b L}{2NH} \sin\left(\frac{2\pi N}{L}(x + L/2)\right) \cos\left(\frac{\pi z}{H}\right), \quad (2)$$

$$u_z = U_b \cos\left(\frac{2\pi N}{L}(x + L/2)\right) \sin\left(\frac{\pi z}{H}\right). \quad (3)$$

U_b is a characteristic velocity scale driven by the rise of the bubbles. We note without proof that this flow field satisfies $\nabla \cdot \mathbf{u} = 0$ everywhere, thus the modeled fluid is incompressible.

A method to numerically solve the advection diffusion equation in time with the given boundary conditions and flow field is desired.

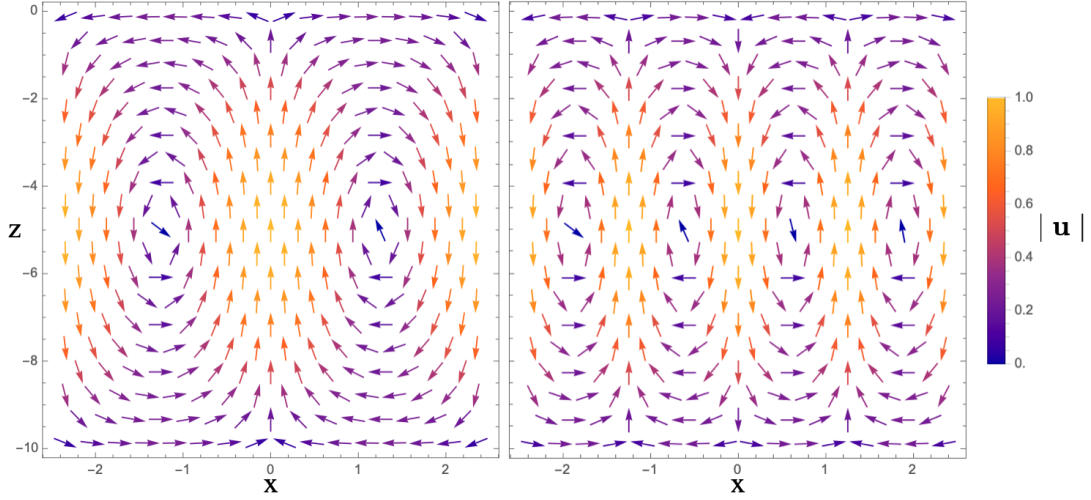


Figure 2: Two fluid velocity fields for a container with $H = 10$ cm, $L = 5$ cm given by equations (2) and (3) for $N = 1$ (left) and $N = 2$ (right).

2.1 Deriving A Finite Volume Method

As we are most interested in the evolution of the concentration of the gas in the fluid, a finite volume method presents itself as the natural approach. Further, a finite volume method will ensure that the gas concentration c is conserved throughout the simulation. We will now proceed with deriving the finite volume method from conservation principles, and show how it relates to a spatial discretization of the advection diffusion equation in (1).

Consider a discretization of our rectangular, two dimensional domain into square cells with side lengths Δx . The corners of the cells are placed at $(x_i, z_j) = (i(\Delta x), j(\Delta x))$ for integers i, j . We use a cell-centered scheme where the flow and concentration quantities are stored at the centroids of the grid cells as shown in figure (3) [8]. With this discretization

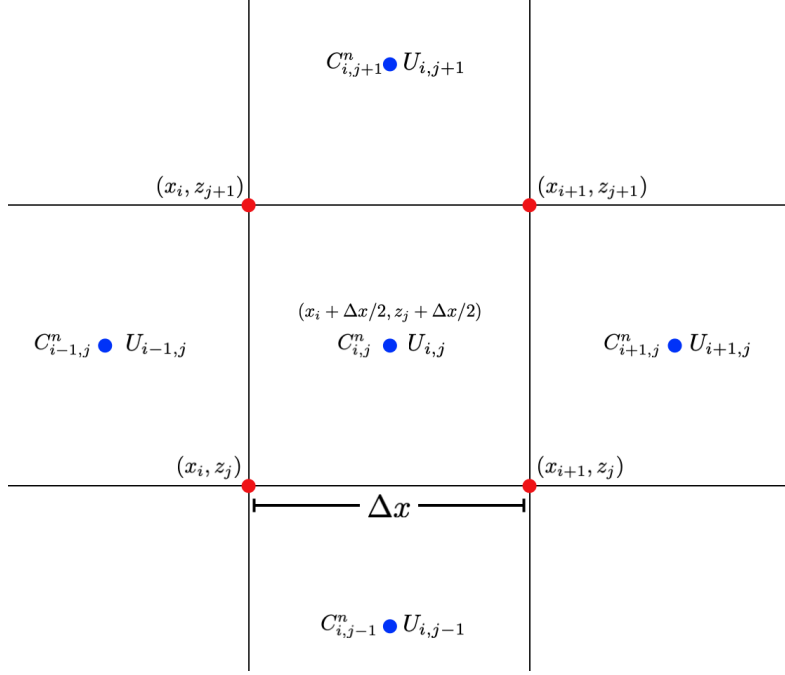


Figure 3: Cell centered discretization scheme. The cell-averaged concentration, $C_{i,j}^n$, and fluid velocity $U_{i,j}$ are stored at the center of the cells (blue). The cell boundaries are the lines formed by the domain discretization, $(x_i, z_j) = (i(\Delta x), j(\Delta x))$ for integers i, j (red).

the control volumes are identical to the grid cells. The integral form of the conservation law for the total concentration of gas in a given cell centered at $\mathbf{x} = (x_i + \Delta x/2, z_j + \Delta x/2)$ is

$$\frac{d}{dt} \iint_{\Omega} c(\mathbf{x}, t) dA = F_{in}(t) - F_{out}(t), \quad (4)$$

Where Ω is the area of the cell, $F_{in}(t)$ and $F_{out}(t)$ are the fluxes of c into and out of the cell at time t . Integrating both sides with respect to time gives the exact formula for the change in c from time t_n to t_{n+1} in the cell.

$$\iint_{\Omega} c(\mathbf{x}, t_{n+1}) dA - \iint_{\Omega} c(\mathbf{x}, t_n) dA = \int_{t_n}^{t_{n+1}} F_{in}(t) dt - \int_{t_n}^{t_{n+1}} F_{out}(t) dt. \quad (5)$$

For our numerical method we will consider the average value of c in each cell

$$\frac{1}{(\Delta x)^2} \iint_{\Omega} c(\mathbf{x}, t_{n+1}) dA - \frac{1}{(\Delta x)^2} \iint_{\Omega} c(\mathbf{x}, t_n) dA = \frac{1}{(\Delta x)^2} \left[\int_{t_n}^{t_{n+1}} F_{in}(t) dt - \int_{t_n}^{t_{n+1}} F_{out}(t) dt \right]. \quad (6)$$

Let $C_{i,j}^n$ be the average value of c in a given cell centered at $(x_i + \Delta x/2, z_j + \Delta x/2)$ and time n , $C_{i,j}^n = (1/\Delta x)^2 \iint_{\Omega} c(\mathbf{x}, t_n) dA$. Moving the second term on the left hand side to

the right gives us an exact equation for $C_{i,j}^{n+1}$ as

$$C_{i,j}^{n+1} = C_{i,j}^n + \frac{1}{(\Delta x)^2} \left[\int_{t_n}^{t_{n+1}} F_{in}(t) dt - \int_{t_n}^{t_{n+1}} F_{out}(t) dt \right]. \quad (7)$$

For sufficiently small Δt we can approximate each of the flux integrals as the flux at time t_n multiplied by Δt :

$$C_{i,j}^{n+1} = C_{i,j}^n - \frac{\Delta t}{(\Delta x)^2} [F_{out}(t_n) - F_{in}(t_n)]. \quad (8)$$

Let the average outwards flux through the left, right, upwards, and downwards faces of the cell at time t_n be denoted by F_l^n, F_r^n, F_u^n , and F_d^n , respectively. Then (8) can be rewritten as

$$C_{i,j}^{n+1} = C_{i,j}^n - \frac{\Delta t}{(\Delta x)^2} [\Delta x (F_l^n + F_r^n + F_u^n + F_d^n)] = C_{i,j}^n - \frac{\Delta t}{\Delta x} [F_l^n + F_r^n + F_u^n + F_d^n]. \quad (9)$$

Now, the fluxes through each face of the cell are due to the advection and diffusion of c , thus we want F_r to be an approximation for the average flux due to advection and diffusion out of the right face of the cell. Since the cell center lies at $(x_i + \Delta x/2, z_j + \Delta x/2)$ the right side face of the cell lies on the line $x_{i+1} = \Delta x(i + 1)$. The average instantaneous flux due to advection out of the right face of the cell at time t_n is then given by given by the integral

$$\frac{1}{\Delta x} \int_{z_j}^{z_{j+1}} u_x(x_{i+1}, z) c(x_{i+1}, z, t_n) dz, \quad (10)$$

where u is the assumed steady state fluid velocity field. Letting $U_{i,j}^x = u_x(x_i + \Delta x/2, z_j + \Delta x/2)$ we can approximate the integrand representing the instantaneous flux with a finite difference approximation using U and C evaluated at the two neighboring cells as

$$u_x(x_{i+1}, z_j) c(x_{i+1}, z_j, t_n) \approx \frac{1}{2} (U_{i,j}^x C_{i,j}^n + U_{i+1,j}^x C_{i+1,j}^n). \quad (11)$$

Since the integral is taken over a length of Δx we arrive at the full approximation for the average flux due to advection through the right boundary of the cell as

$$\frac{1}{2} (U_{i,j}^x C_{i,j}^n + U_{i+1,j}^x C_{i+1,j}^n). \quad (12)$$

By Fick's law the average diffusion of the concentration out of the right boundary of the

cell is equal to

$$\frac{1}{\Delta x} \int_{z_j}^{z_{j+1}} -Dc_x(x_{i+1}, z, t) dz, \quad (13)$$

where c_x is the x component of the gradient of c [9]. Again we can use a centered difference approximation for the gradient to approximate the flux out of the right boundary as

$$-Dc_x(x_{i+1}, z_j, t) \approx -D \frac{1}{\Delta x} (C_{i+1,j} - C_{i,j}). \quad (14)$$

Combining (14) and (12) gives us the approximated average flux out of the right boundary of the cell, F_r , at time t_n

$$\frac{1}{2} (U_{i,j}^x C_{i,j}^n + U_{i+1,j}^x C_{i+1,j}^n) - D \frac{1}{\Delta x} (C_{i+1,j} - C_{i,j}). \quad (15)$$

With the same approach an approximation for F_l at time t_n can be produced, combining both gives the average approximated flux out of the cell in the x directions as

$$\frac{1}{2} (U_{i+1,j}^x C_{i+1,j}^n - U_{i-1,j}^x C_{i-1,j}^n) + D \frac{1}{\Delta x} (-C_{i-1,j} + 2C_{i,j} - C_{i+1,j}). \quad (16)$$

The same method can be used to approximate F_u and F_d to find the average approximated flux out of the cell in the z direction at time t_n .

$$\frac{1}{2} (U_{i,j+1}^x C_{i,j+1}^n - U_{i,j-1}^x C_{i,j-1}^n) + D \frac{1}{\Delta x} (-C_{i,j-1} + 2C_{i,j} - C_{i,j+1}) \quad (17)$$

We finalize our numerical method for calculating the average concentration in the cell centered at (x_i, z_j) at time t_{n+1} , $C_{i,j}^{n+1}$ by replacing $F_l^n + F_r^n + F_u^n + F_d^n$ with the sum of equations (16) and (17) (see the appendix for the full sum). Notably, it becomes clear that the second terms in (16) and (17) are second order accurate approximations to $D\nabla^2 c$ at the point $(x_i + \Delta x/2, z_j + \Delta x/2)$ and time t_n in the x and z directions, respectively. However, The first terms in (16) and (17) slightly differ from a centered difference approximation to $\mathbf{u} \cdot \nabla c$. Our approximation samples \mathbf{u} at the middle cell, $U_{i,j}$, along with the four neighboring cells whereas a second order accurate centered difference approximation of $\mathbf{u} \cdot \nabla c$ at $(x_i + \Delta x/2, z_j + \Delta x/2)$ would only use the value of U at the middle cell. This discrepancy is small and only serves to give a better approximation for the flux due to advection while conserving c . Therefore we expect our finite volume method to produce very similar results to a second order accurate in space finite difference approximation to the advection-diffusion equation in (1).

2.2 Time Stepping

The finite volume method derived in the previous section is only first order accurate in time as equation (9) is essentially using Euler's method to advance from $C_{i,j}^n$ to $C_{i,j}^{n+1}$ by multiplying an approximation to the time derivative of $C_{i,j}^n$ by Δt . We can improve the order of accuracy in time by choosing a higher order linear multistep method. However, a higher order method is not without the cost of significantly increasing the amount of computations done at each time step. As enticing as using RK4 is, it requires computing (16) and (17) four times at each cell along with storing each calculation individually [10]. This increases the computational cost of each time step to the order of $O(4N^2)$ from $O(N^2)$ given by Euler's for a domain consisting of $N \times N$ cells. To keep our simulations more computationally feasible with regards to run time and memory usage we choose to use a second order accurate Adams-Bashforth method which has the form

$$y_{n+2} = y_{n+1} + \Delta t \left[\frac{3}{2}f(y_{n+1}, t_{n+1}) - \frac{1}{2}f(y_n, t_n) \right]. \quad (18)$$

Along with being second order accurate in time, AB2 is an explicit method that leverages the derivative that was calculated at the previous time step to update the solution [10]. Therefore in our implementation, we gain second order accuracy in time while only calculating the time derivative of $C_{i,j}$ at each cell once at every time step. This keeps the computational cost of each time step to $O(N^2)$ operations. Additionally, only two sets of time derivatives for each cell have to be accounted for at any given time, keeping the memory usage to $O(2N^2)$.

When considering the time step size Δt the CFL condition must be satisfied in order for a finite volume method to be stable and convergent [11]. When updating a given cell, our finite volume method only uses the four neighboring cells that share a boundary with the given cell. Therefore we must select Δt such that the gas concentration does not propagate via advection and diffusion a distance larger than Δx at each time step. For the advection term this requires Δt be such that

$$U_{max} \Delta t < \Delta x, \quad (19)$$

where U_{max} is the maximum speed of the fluid among the whole discretized domain,

$$U_{max} = \max_{i,j} \sqrt{u_x(x_i + \Delta x/2, z_j + \Delta x/2)^2 + u_z(x_i + \Delta x/2, z_j + \Delta x/2)^2}. \quad (20)$$

Advancing $C_{i,j}^n$ to $C_{i,j}^{n+1}$ with regards to diffusion is equivalent to multiplying a vector composed of all the $C_{i,j}^n$ values across the whole grid by a matrix A that is Toeplitz. The

non-zero diagonals of A are determined by the five point stencil used in our numerical method for the diffusion term and the values along the diagonals are determined by Δt , Δx , and D . For this to be stable, Δt must be such that all the eigenvalues λ_n of A are $|\lambda_n| \leq 1$. Ensuring this requires calculating the eigenvalues of the N by N matrix A . However, since our diffusion constant, D , is small for the simulations we do not expect this to pose a greater restriction on the size of Δt than the CFL condition for the advection term. To avoid the computational burden of computing the eigenvalues of A which is unlikely to affect our choice of Δt , we consider a proxy for the diffusion restriction given by the one dimensional diffusion problem,

$$D\Delta t < \frac{(\Delta x)^2}{2}. \quad (21)$$

Combining (19) and (21) gives us the complete CFL condition that we ensure Δt satisfies in our computational method:

$$\Delta t < \min\left(\frac{\Delta x}{U_{max}}, \frac{(\Delta x)^2}{2D}\right). \quad (22)$$

Again, in common supersaturated fluids such as carbonated water and beer, the diffusion coefficient is very small thus the CFL condition due to advection is the controlling factor of the size of Δt in our simulations.

3 Codebase

The derived finite volume method was implemented in C++ for performance considerations. The multithreading library OpenMP was used to accelerate the computation of the time derivative of C at each cell in the domain. Ghost cells were used satisfy the zero flux boundary conditions, $\mathbf{n} \cdot \nabla c = 0$, at the sides and bottom of the container. After every time step each ghost cell is updated to have the same value of C as their neighboring interior cell. To satisfy Henry's Law at the air-surface interface, the value of C is set constantly equal to zero at the top most row of cells. For Δt we calculate the right hand side of (22) before each simulation and take Δt to be the resulting value multiplied by 3/4. Since we use a steady state velocity field, the same value of Δt is used for the whole simulation.

4 Results

For the following simulations we use the constant found for U_b in experiments measuring the gas loss of sparkling water performed in [6]. As reported, we take $U_b = 1$ cm/s [6]. Container side lengths measured in cm on the same order as U_b were used in the simulations. For the simulations we take $\Delta x = 0.05$ cm. Different from the true value of initial gas concentration in sparkling water, we set $C^0 = 1$ in each cell. The simulations will still speak to how the gas concentration decays in real supersaturated fluids with different initial gas levels. Although $D = 1.85 \cdot 10^{-5}$ cm²/s for CO₂ in water, we use $D = 0.00925$ cm²/s to make the run time of the simulations required to obtain the full dynamics of the gas concentration more practical. Again, our simulations will speak to the nature of the decay of gas concentration in the fluid, but on a time scale orders of magnitude smaller than physical reality. Movies of a number of simulations discussed in the results are attached to this report and have associated descriptions in the appendix.

4.1 Characterizing The Gas Loss

Plotting the average concentration \bar{C} over time reveals consistent exponential decay in the gas concentration. Figures (4) and (5) plot the average gas concentration over time for a range of different container sizes and number of circulation cells, all revealing exponential decay. In the first roughly five seconds, the gas decays at a slightly faster rate than the rest of the simulation as seen in figure 4(b) for a single circulation cell. This is due to the initial uniform concentration just below the boundary layer that immediately diffuses across the air surface interface. As the bubbles drive the circulation flow with a characteristic velocity on the order of 1 cm/sec, the circulation cell gains structure in the first ten seconds. This results in lower concentration along the sides of the container near the surface where the fluid is flowing downwards and consistently well mixed concentration from the bulk near the surface in the middle of the container where the fluid is ascending. Once the circulation cell has fully formed after this roughly ten seconds most of the gas loss is occurring in the center of the container while little is lost near the edges, giving rise to the consistent exponential decay for $t > 10$. For flows with more than one circulation cell, the same behavior is seen. Fitting the data in figure 4(a) to the function $y(s) = e^{-1.2(Ds)}$ produces a nearly indistinguishable plot, confirming the exponential decay in the average value of C .

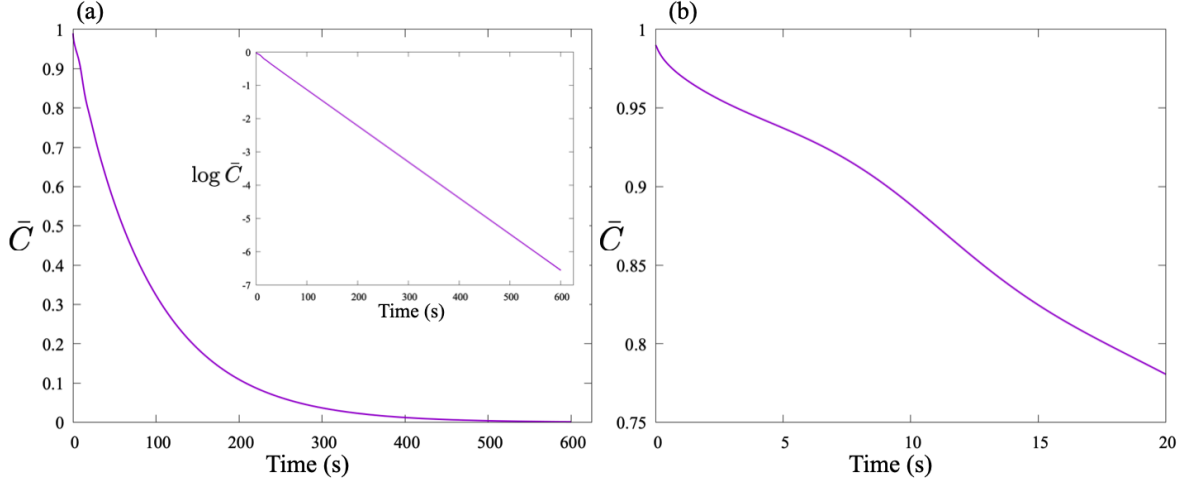


Figure 4: (a) The average cell gas concentration \bar{C} during the first 500 seconds of the simulation for a container with $L = 5$ cm, $H = 5$ cm, supporting a single circulation cell, $N = 1$. Inset: The same, on a log-linear scale. (b) The average cell gas concentration \bar{C} during the first 20 seconds of the simulation for the same parameters as (a).

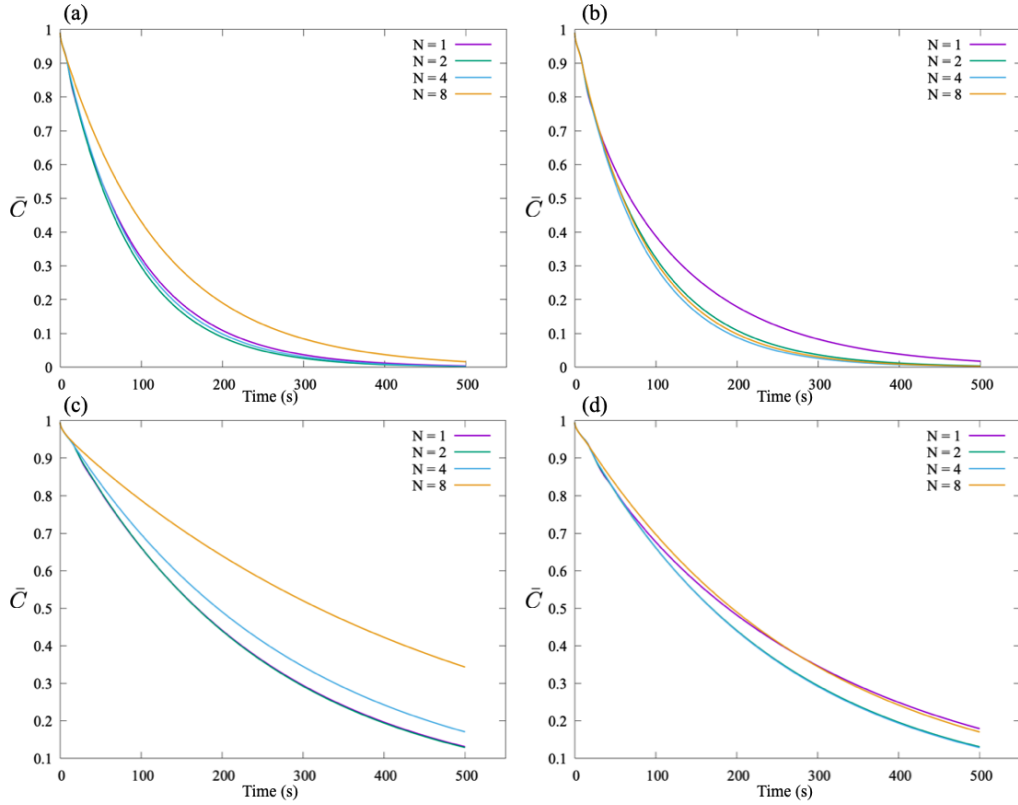


Figure 5: The average gas concentration \bar{C} over time for a range of container geometries and number of circulation cells, N . (a) $L = H = 5$ cm. (b) $L = 10$ cm, $H = 5$ cm. (c) $L = 5$ cm, $H = 10$ cm. (d) $L = H = 10$ cm.

4.2 Circulation Cells

The group initially hypothesized that increasing the number of circulation cells inside the container would steadily increase the rate of gas loss, perhaps up to a certain number of cells. Each circulation cell acts as conveyor belt, advecting concentration from the bulk liquid directly to the top of the container for it to diffuse across the air-surface interface thus it seemed plausible that increasing the number of circulation cells would increase the rate of gas loss. However, as shown in figures (5) and (6), the geometry of the container plays a decisive role in how increasing the number of circulation cells changes the rate of gas loss.

While holding the dimensions of the container constant, increasing the number of circulation cells decreases the horizontal length of regions in the container where the fluid is flowing in the same vertical direction. As seen in figure (6), this allows the flow with one circulation cell to have the largest flow channels on the sides and center of the container. The increase in the horizontal length of the flow channels enables the circulation cell to distinctly form. Comparing figure 6(a) to figure 6(d) reveals this distinction. In figure 5(a) the single cell's two flow channels clearly form across the whole vertical length of the container, allowing concentration from the low velocity flow regions near the center of the two vortices to steadily diffuse into the faster regions and be carried to the surface. For $H = L = 5$ cm, this factor of flow channel width begins to inhibit the gas loss for $N > 5$ as seen in figure 5(a) where the case of $N = 8$ displays a significant decrease in the rate of gas loss. Increasing the horizontal length of the container compensates for this effect. In figure 5(b) where $L = 10$ cm, $H = 5$ cm the increase in the number of circulation cells provides enhanced gas loss for $N = 2, 4, 8$ as compared to a single circulation cell. Expectedly, increasing the height of the container diminishes the rate of gas loss regardless of the number of circulation cells. This can be simply explained by the fact that a deeper container allows for much more fluid in the well mixed concentration far away from the surface, keeping the average concentration \bar{C} at a larger value over time. While for $H = L = 5$ cm, the cases of $N = 2, 4$ lose gas slightly faster than the single circulation cell, increasing H to 10 cm removes that advantage (figure 5(c)). The increased container height provides much more fluid that the cells must circulate vertically, and for increasing N the width of the flow channels decreases substantially. Further, as the characteristic velocity of the flow field is kept constant, it takes twice as long for a volume of fluid to travel from the bottom of the container to the surface. These factors coupled together slow down the large scale mixing of high and low concentration areas, inhibiting the decrease in \bar{C} significantly for the simulations with more circulation cells. Evening out the length and width of the container such that $H = L = 10$ cm again remediates some of the slowed down gas loss for $N = 4, 8$ as seen in figure 5(d).

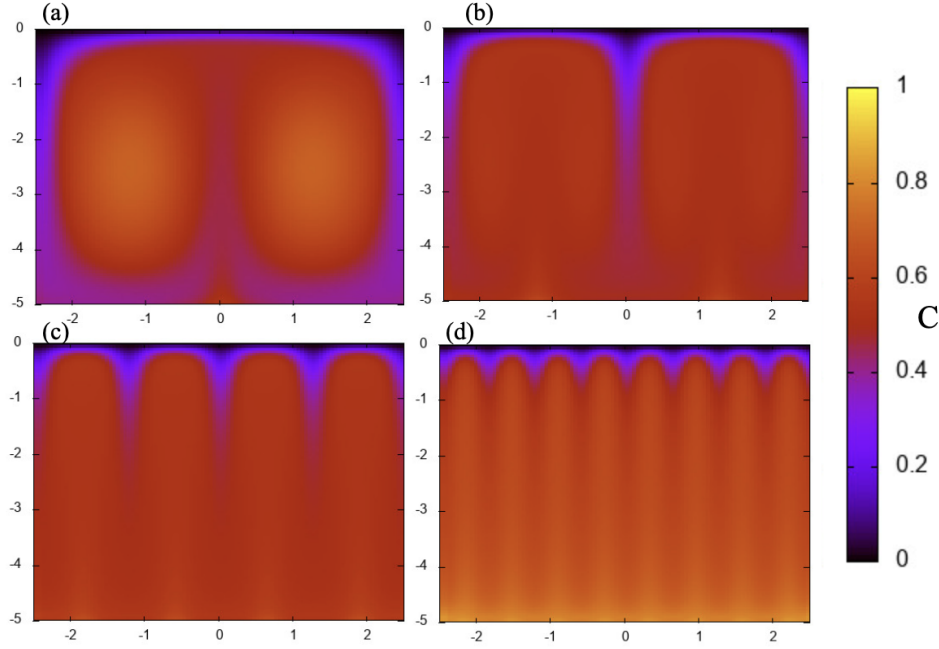


Figure 6: The gas concentration in the container at $t = 60s$ with $H = L = 5$ cm for (a) $N = 1$, (b) $N = 2$, (c) $N = 4$, and (d) $N = 8$ circulation cells.

Figure (7) shows the development of the distribution of gas concentration in a container supporting a single circulation cell. As discussed above, on a timescale of the bubble velocity U_b , the circulation cell develops the distribution where there is lower gas concentration along the flow channels and higher concentration in the two low velocity regions at the center of the vortices. These two regions grow more distinct in time as the boundary layer near the surface slightly increases in vertical length in the center while growing significantly larger at the sides. This decrease in the average gas concentration near the surface leads to fluid containing little gas concentration being advected down the sides and to the bottom of the container, encircling each region of higher gas concentration and low fluid velocity. As seen in figure (7) this distribution of gas concentration fully forms by $t = 30$ seconds. After this distribution takes shape, the higher gas concentration in the low velocity regions near the center of the vortices slowly diffuse into the surrounding flow channels that carry the gas to the surface to be released.

A characteristic length scale that emerges from the data is the ratio of the horizontal length of the container compared to the vertical length of the container, L/H . As L/H decreases while the total fluid volume is held constant the rate of gas loss inferred by measuring \bar{C} diminishes as the the air-liquid interface where the gas leaves the fluid decreases in size. Figures 5(b) and 5(c) confirm this relationship, revealing the decrease in the rate of gas loss between $L/H = 2$ and $L/H = 1/2$, respectively.

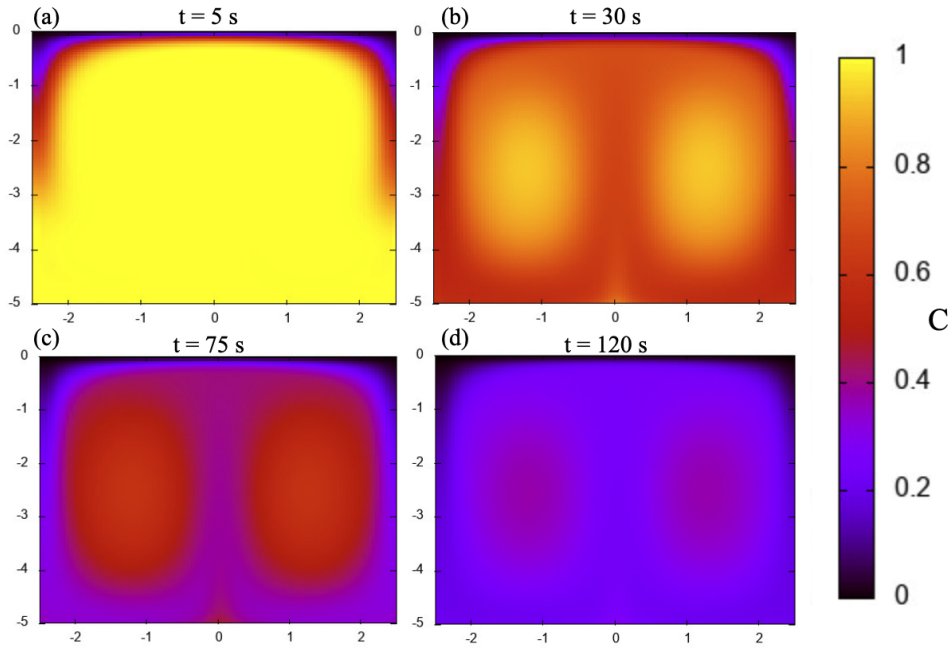


Figure 7: The gas concentration in the container with $H = L = 5$ cm and a single circulation cell, $N = 1$ for times (a) $t = 5$ s, (b) $t = 30$ s, (c) $t = 75$ s, and (d) $t = 120$ s.

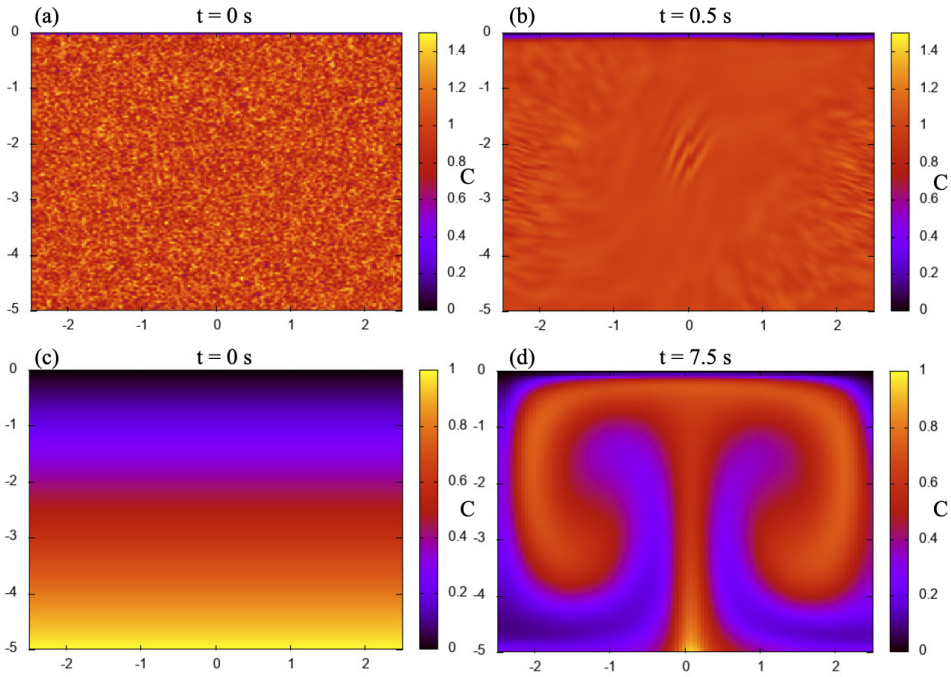


Figure 8: The gas concentration in the container with $H = L = 5$ cm and a single circulation cell, $N = 1$ for times (a) $t = 5$ s, (b) $t = 30$ s, (c) $t = 75$ s, and (d) $t = 120$ s.

4.3 Non-Uniform Initial Concentration

Running the simulation with different non-uniform initial gas concentrations reveals how both the advective and diffusive terms in the governing PDE bring the system to the same well mixed state reached by the simulations with uniform initial concentration. In figures 8(a) and 8(b) the initial concentration in each cell is taken as $C^0 = 1 + (1/2)\text{Rand}(-1,1)$ where $\text{Rand}(-1,1)$ is a random number in $(-1, 1)$. This produces an initial average concentration near $\bar{C} = 1$ with random fluctuations up to magnitude $1/2$ around 1. Figure 8(b) shows how the diffusion immediately begins to smooth out the concentration in under a second. In the center of the container the fluid velocity begins to advect the small fluctuations in the concentration generated by the diffusion. This creates the small, angled waves in the concentration seen in the center of figure 8(b). In a matter of a few seconds the concentration throughout the whole container is very close to uniform and the simulation becomes indistinguishable from an initially uniform concentration simulation.

In figures 8(c) and 8(d) the simulation is performed with a vertical gradient in the initial concentration where C^0 ranges from zero near the surface to one at the bottom of the container. This initial condition represents a supersaturated fluid switching from a purely diffusive process to introducing advection with a suddenly developing fluid velocity field. The introduced advection mixes the fluid on the time scale of the bubble velocity, $U_b = 1$. The fluid containing high gas concentration is brought to the surface, significantly increasing rate of gas loss within a few seconds. Vortexes circulating two distinct areas of high and low concentration fluid are formed by the circulation flow. In these vortexes the two concentrations remain distinct for roughly twenty seconds before diffusion mixes them into one higher concentration region as seen in the two low velocity regions in figure 7(c). Past $t = 20$ s the simulation evolves identically to one with an initially uniform concentration.

5 Discussion

The relationship between the container shape and number of circulation cells is more complex than initially hypothesized. From figures (5) and (6) it's clear that it is not a simple correlation where increasing the number of circulation cells while maintaining the same container geometry increases the gas loss. Further, our simulations infer that for each container geometry, there is an optimal number of circulation cells to maximize the rate of gas loss from the fluid. This prompts the idea of designing containers meant to hold supersaturated fluids (cans, glasses, barrels, etc...) with specific geometries for

the purpose of encouraging or inhibiting gas loss. High quality Champagne glass are etched on the inside of the glass to encourage bubble growth [4]. A similar idea could be used to encourage bubble growth in specific locations on the bottom of the container, possibly controlling how many circulation cells form upon opening the container and the subsequent rate at which the fluid loses gas.

There are two timescales that affect the degassing of the fluid, seen in figure (7). The short timescale comes from the characteristic bubble velocity U_b , and determines the rate at which non-uniform gas distribution grows. On this timescale the initial boundary layer at the surface forms, and gas concentration that was initially residing on the flow channels is continuously advected around the circulation cell and diffused across the surface. Figure 7(b) shows how after thirty seconds the gas concentration along the flow channels and near the surface has significantly decreased to an average around $C \approx 0.6$ from the initial concentration $C = 1$. The much longer time scale is determined by the diffusion coefficient, D . It is on this time scale that the gas diffuses from the low velocity regions in the center of the vortexes into the flow channels for it to be carried to the surface, as seen in the gas distribution in figure 7(c). Though the advection time scale drives a significant amount of gas loss at early times, the diffusion time scale determines the rate at which most of the gas is removed.

The limitation on the gas loss from the constant, slow velocity regions outside of the flow channels prompts the idea that regular fluctuations in the velocity field would serve to significantly enhance the rate of gas loss. Small fluctuations in the velocity field would allow for gas concentration in the large regions near the center of the vortexes to occasionally be advected into the flow channels and subsequently to the surface instead of having to wait to diffuse into the flow channel.

Interesting directions to continue this work include expanding the model to three dimensions, numerically solving Navier Stokes, and investigating non-rectangular containers.

References

- [1] W. Henry, “Experiments on the quantity of gases absorbed by water, at different temperatures, and under different pressures,” *The Royal Society*, pp. 29–42, 1803.
- [2] P. S. Epstein and M. S. Plesset, “On the stability of gas bubbles in liquid-gas solutions,” *J. Chem. Phys.*, vol. 18, no. 11, pp. 1505–1509, 1950.
- [3] L. E. Scriven, “On the dynamics of phase growth,” *Chem. Eng. Sci.*, vol. 10, no. 1-2, pp. 1–13, 1959.
- [4] G. Liger-Belair, “The physics behind the fizz in champagne and sparkling wines,” *Euro. Phys. J. Special Topics*, vol. 201, no. 1, pp. 1–88, 2012.
- [5] L. Pereira, F. B. Wadsworth, J. Vasseur, M. Schmid, S. Thivet, R. B. Nuernberg, and D. B. Dingwell, “The physics of dancing peanuts in beer,” *Roy. Soc. Open Sci.*, vol. 10, no. 6, p. 230376, 2023.
- [6] S. Spagnolie, S. Christianson, and C. Grote, “Dancing raisins: levitation and dynamics of bodies in supersaturated fluids,” *arXiv preprint arXiv:2308.12927*, 2023.
- [7] G. Liger-Belair, “The physics and chemistry behind the bubbling properties of champagne and sparkling wines: A state-of-the-art review,” *J. Agric. Food Chem.*, vol. 53, pp. 2788 – 2802, 2005.
- [8] J. Blazek, *Computational Fluid Dynamics: Principles and Applications*. Elsevier, 2005.
- [9] A. Fick, “On liquid diffusion,” *The London, Edinburgh, and Dublin Philosophical Magazine and Journal of Science*, 1855.
- [10] E. Süli and D. Mayers, *An Introduction to Numerical Analysis*. Cambridge University Press, 2003.
- [11] R. LeVeque, *Finite Difference Methods for Ordinary and Partial Differential Equations*. Society for Industrial and Applied Mathematics, 2007.

6 Appendix

6.1 Full Numerical Method

The full finite volume method for updating the concentration in a given cell $C_{i,j}^n$ from t_n to t_{n+1} is:

$$C_{i,j}^{n+1} = C_{i,j}^n - \frac{\Delta t}{2\Delta x} (U_{i,j+1}^z C_{i,j+1}^n - U_{i,j-1}^z C_{i,j-1}^n + U_{i+1,j}^x C_{i+1,j}^n - U_{i-1,j}^x C_{i-1,j}^n) - D \frac{\Delta t}{(\Delta x)^2} (-C_{i,j-1} + 2C_{i,j} - C_{i,j+1} - C_{i-1,j} + 2C_{i,j} - C_{i+1,j})$$

6.2 Second Order Time Accuracy

Second order Adams-Bashforth was used for time stepping. Let $C_{i,j}^N$ be our numerical solution to $c(x_i, z_j; T)$ produced by taking N time steps between $t = 0$ and $t = T$. For our method to be second order accurate in time we would expect that $C_{i,j}^N$ is of the form:

$$C_{i,j}^N = c(x_i, z_j; t_n) + O((\Delta t)^2). \quad (23)$$

Similarly for $2N$ and $4N$ we would expect that $C_{i,j}^{2N} = c(x_i, z_j; t_n) + O((\Delta t/2)^2)$ and $C_{i,j}^{4N} = c(x_i, z_j; t_n) + O((\Delta t/4)^2)$, respectively. Therefore, for a fourth order accurate algorithm we expect that

$$\frac{C_{i,j}^N - C_{i,j}^{2N}}{C_{i,j}^{2N} - C_{i,j}^{4N}} = \frac{k^4 - (k/2)^4}{(k/2)^4 - (k/4)^4} = 2^2. \quad (24)$$

We now use this method to analyze our algorithm. We take $L = H = 5$, $T = 10$, $i = LL/2 + 10$, and $j = HH/2 - 10$ where L and H are the number of cells utilized in the x and z directions, respectively. This produced a value of 4 as expected, inferring second order accuracy in time.

6.3 Movies

- **M1.mp4:** $L = H = 5$ cm, $N = 1$, for 120 seconds.

- **M2.mp4:** $L = H = 5$ cm, $N = 8$, for 100 seconds.
- **M3.mp4:** $L = 10$ cm, $H = 5$ cm, $N = 1$, for 100 seconds.
- **M4.mp4:** $L = 10$ cm, $H = 5$ cm, $N = 2$, for 100 seconds.
- **M5.mp4:** $L = 5$ cm, $H = 10$ cm, $N = 1$, for 100 seconds.
- **M6.mp4:** $L = 5$ cm, $H = 10$ cm, $N = 8$, for 100 seconds.
- **M7.mp4:** $L = H = 10$ cm, $N = 1$, for 100 seconds.
- **M8.mp4:** Random fluctuations in initial concentration with $L = H = 5$ cm, $N = 1$, for 20 seconds.
- **M9.mp4:** Gradient initial concentration with $L = H = 5$ cm, $N = 1$, for 40 seconds.